The Role of Moment Tensors in the Characterization of Hydraulic Stimulations

Ismael Vera Rodriguez, James Rutledge and Sergey Stanchits

Keywords Moment tensor · Microseismic monitoring · Acoustic emission Hydraulic stimulation

1 Introduction

Hydraulic stimulation is a technique aimed at increasing the effective permeability of rock reservoirs in connection to a producing/injecting well (Economides and Nolte 2003). It is applied in the oil and gas industry to increase production in unconventional reservoirs, and in geothermal systems to enhance fluid circulation. This technique (similar to others involving the injection of fluids such as CO_2 sequestration, natural gas storage and wastewater disposal) has the potential to induce small seismic events (generally with moment magnitude $M_w < 0$). The analysis of this induced microseismicity is of interest for purposes ranging from seismic hazard assessment to reservoir characterization.

In the oil and gas industry, hydraulic stimulations start with the high pressure injection of a water-based fluid. The process stimulates the reservoir by driving extension fractures from the injection point into the rock formations. This results in the creation and activation of new and pre-existing fractures. New and pre-existing fractures can be activated in combinations of tensile, compressive, and shear modes depending on the state of stress, the rock's fabric and strength, and pore-pressure coupling into the rock. Furthermore, as a side effect, some of these fractures also release

I. Vera Rodriguez (✉)
Schlumberger Cambridge Research, High Cross, Madingley Road, Cambridge CB3 0EL, UK
e-mail: verarodr@ualberta.ca

J. Rutledge
Schlumberger, 3750 Briarpark Drive, Houston, TX 77042, USA

S. Stanchits
Formerly at Schlumberger Research, 6350 West Sam Houston Pkwy N, Suite 200, Houston, TX 77041, USA

S. D'Amico (ed.), *Moment Tensor Solutions*, Springer Natural Hazards,
https://doi.org/10.1007/978-3-319-77359-9_8

seismic energy that we observe as microseismic activity. After fracture extension reaches a region away from the injection point, a propping agent is pumped down to pack-open the fracture planes that are connected with the wellbore to retain a high permeability path between the reservoir and the treated well after pumping has ceased (Fink 2013). Connectivity, asperities, tortuosity and settling effects, however, are expected to prevent the proppant from reaching every open fracture within the stimulated volume, especially in systems of fractures with planes that are connected at high angles (McLennan et al. 2008). At the end of the injection, when the pressure is reduced at the wellbore, the fracture(s) that are not supported by proppant close again. Therefore, the volume of rock containing proppant is normally smaller than the total stimulated volume (Mayerhofer et al. 2010). Some self-propping of the fracture system is also expected due to shear dislocations along irregular surfaces or at fracture discontinuities, but production enhancement obtained from the hydraulic stimulation is arguably coming primarily from the propped volume. For this reason, it is of great interest to obtain a picture of the stimulated fracture network, proppant transportation and proppant placement. Because the effective fracture network contributing to production is influenced by multiple variables including local, poorly known factors such as the rock's fabric and strength, the effectiveness of hydraulic stimulations can vary within a few tens of meters. This variability introduces the need for methodologies that permit a cost-efficient and reliable characterization of fracture growth and deformation for individual stimulation treatments.

Among the different diagnostic techniques available to characterize hydraulic stimulations, microseismic monitoring has been one of the most versatile and successfully applied (Cipolla and Wright 2002). Microseismic monitoring consists of the recording and analysis of the seismic energy released from the activation of some of the fractures stimulated by hydraulic injections. The monitoring is conducted with arrays of receivers deployed on the surface of the earth and/or inside shallow or deep boreholes (Duncan and Eisner 2010; Maxwell et al. 2010). From the analysis of the spatial locations of the microseismic events, information can be extracted regarding the geometry of the stimulated volume (e.g., Bennett et al. 2005), and the complexity of the stimulated fracture network (Cipolla et al. 2008). Combining spatial and temporal information, microseismic events have been used to obtain estimations of the permeability tensor of the fracture network (Shapiro et al. 1999), and to detect proppant bridging (Maxwell et al. 2004). The source spectrum of microseismic arrivals provides information about the seismic moment and corner frequency, which are useful for estimating event magnitudes, source dimensions, stress drops and radiated seismic energy. Graphs of cumulative seismic moment release can quantify seismic-measured deformation, uncovering interactions between small fracture networks and larger faults being activated by the hydraulic treatment (Rutledge et al. 2004; Maxwell et al. 2008). Moment-derived magnitudes (M_w) are also the basis of traffic-light systems used to control the size of events during injection operations (e.g., Department of Energy and Climate Change 2014). Stress drops derived from seismic moments and corner frequencies have been interpreted to reflect stress heterogeneities during fracture growth and help to discriminate between fluid-induced

and stress-related activation of microseismic events (e.g., Urbancic and Rutledge 2000; Goertz-Allmann et al. 2011).

Moment tensor inversion, or MTI, describes the inelastic deformation of the source region that generates the microseismic signal. In earthquake seismology, the source mechanism is usually presented as a "fault-plane solution", providing the fault's orientation and the slip vector direction (rake). The fault-plane solution is also commonly referred to as the double-couple (DC) solution, which is a special case of the moment tensor (MT) that assumes that the signal is generated from shear dislocation along a planar surface in an isotropic medium. More generally, the MT can describe multiple other source types. For example, internal sources such as explosions/implosions, crack opening or closure, slip on a plane, or any combination and superposition of these are represented by symmetric MTs. The MT's general decomposition into displacement discontinuity sources, describing fracture deformation in anisotropic media, is described in Chapman and Leaney (2012), Leaney et al. (2014), and Vavryčuk (2015). Since hydraulic-stimulation microseismicity is generated by high-pressure injection of fluids, one of the primary interests in MTI is the distinction of fracture tensile/closure events from shear displacements.

MTI provides useful information on the geomechanical response of a reservoir to the hydraulic stimulation. In principle, MTI provides a partial description of how a fracture system, pre-existing, created and/or augmented through growth, is responding to some in situ stress field that is being altered by the injection. Additional information helpful in interpreting MTI results includes analyses of source locations with respect to the geology, target reservoir, and stress magnitudes and orientations. Also, natural fracture characterization, and the correlation between the temporal development of the seismicity and injection parameters provide useful context and input to MT interpretation. Generally, MTI results can be a reference to build and calibrate fracture models. Specifically, MTI can provide statistics on fracture orientations, indicate areas of volume creation, and by inference, the mapping of proppant placement (e.g., Neuhaus et al. 2014; Yu et al. 2015).

Events predominantly exhibiting shear mechanisms are common during hydraulic stimulations. Stress anisotropy in the earth's crust creates shear stresses. Since a rock's shear strength is typically greater than its tensile strength, shear stress is easier to sustain in the earth, and can be released when pore pressure during injection reaches some threshold value (e.g., as critical failure of the rock or slip along pre-existing fractures). Shear stresses are also generated near the tip of a tensile crack, which may also drive rock to shear failure just ahead of the hydraulic fracture. Conversely, tensile stresses are induced near the tips of shear cracks, so, in general, shear and tensile fracturing are closely coupled phenomena. Although microseismicity may under-represent the gross deformation occurring during hydraulic fracturing, MTI analysis provides an important measure of the geomechanical response to hydraulic stimulation.

In addition to the calibration of fracture networks, MTs have other applications in microseismic monitoring. For example, the seismic moment of a microseismic event can be predicted using source models developed in global seismology (e.g., Aki 1966) or from the normalization of its estimated MT. Source models in global

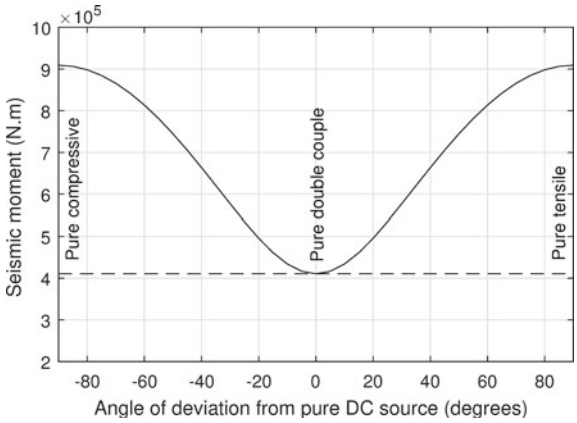

Fig. 1 Comparison of seismic moment (M_0) predictions from MT normalization (solid line) and a source model that assumes pure DC (dashed line). The medium is isotropic with Vp = 3633 m/s, Vs = 2142 m/s and $\rho = 2700$ kg/m^3. The fracture area is 1 m^2 and the stress drop $\Delta\sigma = 1$ MPa. The fracture plane is vertical, activated with a rake of 0° (strike-slip shear displacement in the pure DC case)

seismology often include the implicit assumption of a pure DC source in isotropic, homogeneous media (e.g., Brune 1970). In hydraulic stimulations, however, non-DC dislocations have been identified both at field and laboratory scales (e.g., Sileny et al. 2009; Vera Rodriguez et al. 2017), while most of the microseismicity of interest takes place in anisotropic formations such as shales. The seismic moment of a non-DC dislocation is systematically underestimated when computed with traditional source models that assume pure DC (Fig. 1). For this reason, seismic moment from MT normalization gives a more general approximation for the expected size of a microseismic event. The source types interpreted from MTs provide an insight into the local state of stress, where the variability of the source types can be directly linked to the complexity of the stress field at a specific snapshot in time and space (e.g., Aker et al. 2014). More recently, the evolution of fracture geometries and styles of activation obtained from MTs has received increased attention with the objective to gain a better understanding of the mechanics of hydraulic stimulations (e.g., Tan and Engelder 2016; Rutledge et al. 2016).

In this chapter, we illustrate two applications of MT analysis related to the study of hydraulic stimulations. Both applications study the mechanics of the problem at different scales. In the first case, field-scale data are analysed to develop an understanding of fracture propagation and its interaction with formation bedding. In the second application, the MTs of acoustic emissions observed in a laboratory experiment are analysed to develop an understanding of the source types that can be expected during hydraulic stimulations at field-scale.

2 Characterization of a Field-Scale Hydraulic Stimulation Through the Moment Tensors of Microseismicity

The growth of hydraulic fractures in layered sedimentary rocks is strongly controlled by the mechanical stratigraphy. The mechanical discontinuities and stress contrast across layer interfaces tend to impede vertical growth relative to lateral extension, allowing the creation of reservoir-contained fractures that extend laterally up to hundreds of meters (Chuprakov and Prioul 2015). Not surprisingly, the occurrence and mechanisms of microseismicity induced during hydraulic fracturing can also be controlled by mechanical stratigraphy. Precise microseismic source locations sometimes show fine-scale banding of events in depth (e.g., Rutledge et al. 2004, 2015), implying brittle deformation in some layers and stable, aseismic extensional growth in others. The elastic heterogeneity associated with the stratigraphy can explain the banding of events (e.g., Langenbruch and Shapiro 2014; Roche and van der Baan 2015). Depending on specific conditions, one could invoke a number of mechanisms to explain such correlations. For example, stiffer layers can support higher stress magnitudes and higher differential stresses, which can control the occurrence of natural fractures.

Dip-slip microseismic mechanisms are commonly observed during hydraulic fracture stimulations in shales in which vertical nodal planes tend to be aligned with the expected hydraulic-fracture orientation. Various investigators have suggested that the events represent shearing on bedding planes with the alternate, horizontal nodal plane corresponding to the slip surface (e.g., Rutledge et al. 2013; Stanek and Eisner 2013). We present a few cases of such observations and present a simple argument for bedding-plane slip rather than vertical dip-slip mechanisms. We then invoke a simple model of Chuprakov and Prioul (2015) to explain the persistent mechanisms. In their model, tensile crack vertical-growth can arrest at weak bedding interfaces. Fluid invasion and pressure can weaken the interface which can then shear from the added stress of adjacent crack opening. Under certain conditions, with subsequent net pressure recovery and gain at the weak interface, the parent tensile fracture propagation can continue across the interface. In one case presented here for a stimulation treatment in the Barnett shale, invoking this model qualitatively provides a consistent explanation of the continuity and time-space development of the microseismic structures, as well as explaining the observed patterns of shear-fracture first motions.

2.1 Observations

Figure 2 shows an example of the interpretation of surface microseismic data collected during a multi-well, multi-stage completion program in a shale reservoir. An extensive array of shallow-well geophone receivers allows the determination of the MTs. Within the encircled area, the mechanisms are fairly uniform dip-slip events with the near vertical nodal planes aligned close to the event trends and expected

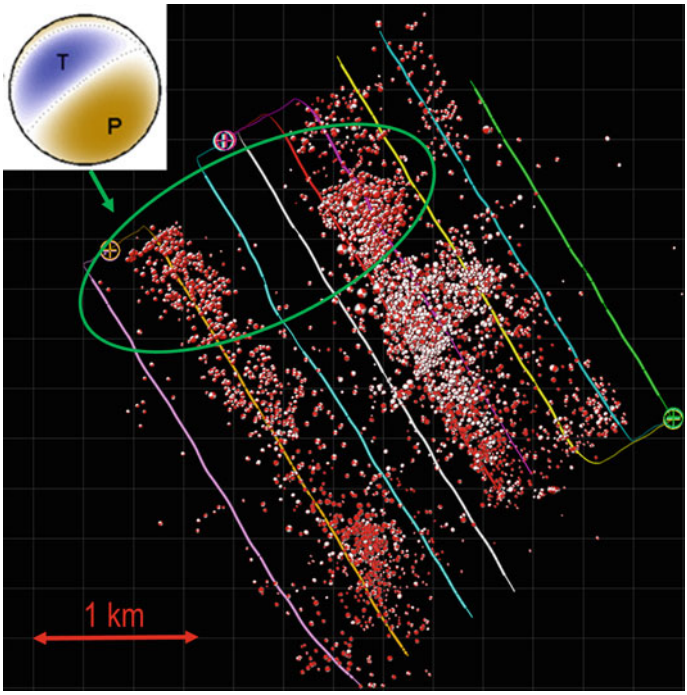

Fig. 2 Example of surface microseismic data from well completions in a shale reservoir. Events were detected on a grid array of 47 shallow-well receivers. Events are displayed showing upper hemisphere first motions. Within the green ellipse most events show dip-slip mechanisms on steep planes striking subparallel to the event trend and expected maximum horizontal stress (SHmax) direction. The inset solution is a high signal-to-noise ratio example from within the green ellipse. The alternate nodal plane is near horizontal

SHmax direction (Fig. 2). Similarly aligned and persistent mechanisms in shale reservoirs are also revealed in cases presented by Stanek and Eisner (2013) and Diller et al. (2015).

Figure 3 shows a similar population of mechanisms from downhole data in another shale reservoir. The data were acquired using multiple monitor wells so that the full MTs are well constrained. The events are primarily shear mechanisms showing predominantly dip-slip displacements on fractures aligned with the hypocenter trend and principal stress direction. Steeply dipping natural fractures over the same depth interval are sparse with orientations widespread and poorly correlated with the uniform vertical nodal plane orientations exhibited by the source mechanisms (Figs. 3 and 4).

Sometimes such aligned and repetitive mechanisms can be inferred from composite patterns of P- and S-wave first motions and amplitude ratios observed from a single vertical monitor well (Rutledge and Phillips 2003; Rutledge et al. 2013). An example of this is shown in Fig. 5 from the Barnett shale, where a persistent radiation

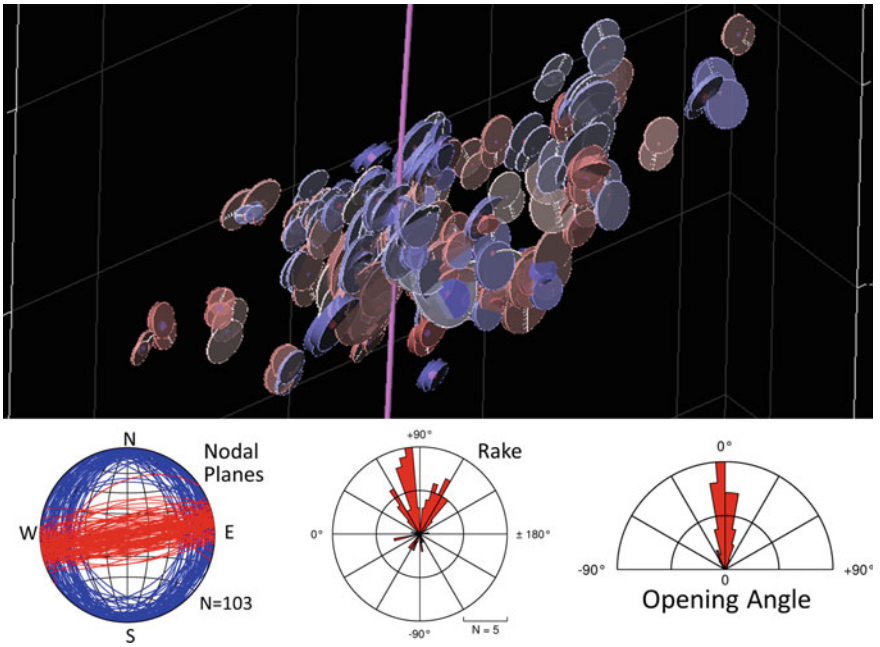

Fig. 3 Perspective view of a microseismic cloud (top). The cloud length is about 300 m, and height is about 150 m. The treatment well is vertical (purple line). The event glyphs represent the MT decompositions (see Leaney et al. 2014), where the displacement between the two disks portrays the component of slip and the disk thickness represents the tensile component, colored red for opening and blue for closing. For display purposes, a minimum disk thickness is required for a pure slip source. The radii of the disks scales with the moment scalar. The stereonet and rose diagrams summarize the geometry of the source mechanisms that show dip-slip displacements (73% of solutions shown in the perspective view), where the red nodal planes correspond to the glyph orientations. The vertical planes have a mean strike of $81° \pm 8°$, mean dip of $90° \pm 13°$ and are oriented subparallel to the hypocenter trend and principal stress direction (~92°). The mean opening angle is $-1.0° \pm 12°$ indicating they are primarily shear mechanisms. The opening angle would be 0° for a pure slip source and $\pm 90°$ for a pure opening (+) or closing (–) crack (Chapman and Leaney 2012). The remaining mechanisms represented in the perspective view (27%) are similarly oriented strike-slip events. Mean condition number is 5.4 ± 0.3

pattern is revealed by the pattern of P- to SH-wave amplitude ratios with respect to the monitor-well azimuthal position. The systematic radiation pattern corresponds to a dip-slip mechanism with a vertical nodal plane striking ~50°, close to the event trend and regional maximum horizontal stress (SHmax) direction.

The source locations shown in Fig. 5 were determined precisely using correlated picks and the method outlined by Rutledge and Phillips (2003). The mean rms residual is 0.2 ms. The gross geometry resolved are two vertical fractures, about 150 ft apart, growing simultaneously from the isolated perforation intervals. The depth locations form distinct bands separated by aseismic intervals. A gap of event detection is evident on the two depth projections near the origin of the horizontal distance-along-

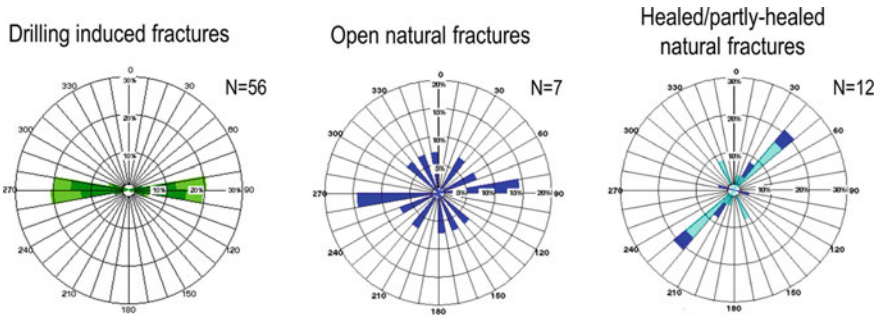

Fig. 4 Summary of borehole fracture image logs obtained in a well adjacent to the treatment well of Fig. 3, and covering a 260 m interval of the reservoir. SHmax inferred from drilling induced fractures is east-west parallel to the event trend. Natural fracture counts and strikes are for fracture dips >80°. The natural fracture count is low over the 260 m interval and shows poor correlation with the vertical nodal planes of Fig. 3

strike axis (Fig. 5). The gap is the result of signal loss at the SH-nodal azimuth with respect to the vertical receiver array, and our selection criteria of requiring clear P- and S-wave signals for precise locations.

The sequence of events and their general vertical alignment suggest through-going, vertical hydraulic fractures. Figure 6 shows the spatio-temporal development of the two resolved fracture zones. Most of the microseismicity is occurring at or near the leading edges, especially for the south fracture. The gap of events from about 800 to 1000 ft distance in Fig. 6 again corresponds to the SH-nodal azimuth. Fracture height comprising the lower two active intervals is established early and these intervals grow together laterally (red and blue symbols, Fig. 6). Upward growth to the shallowest interval occurs late (green symbols), but it also shows most of the seismicity is on the corresponding leading line moving laterally from the perforations.

2.2 Bedding Plane Slip in Shale Reservoirs

Injection-induced seismicity is often explained in terms of the Mohr diagram, where increased pore pressure reduces the effective normal stress and drives the rock closer to failure. For hydraulic-fracture microseismicity, this would correspond to driving the surrounding rock to failure via leak off and pressure coupling through the matrix or by direct connection into natural fracture networks. Our observations of nodal planes prevalently aligned close to the corresponding principal stress are difficult to reconcile with the Mohr diagram. In most cases, promoting shear preferentially at low angles to maximum stress is difficult without first crossing failure conditions for a much broader aperture of orientations (Rutledge et al. 2015). Further, matrix permeability of shales are typically extremely low, and natural fractures can be sparse and not necessarily aligned with principal stress (for example, Figs. 3 and 4). Thus,

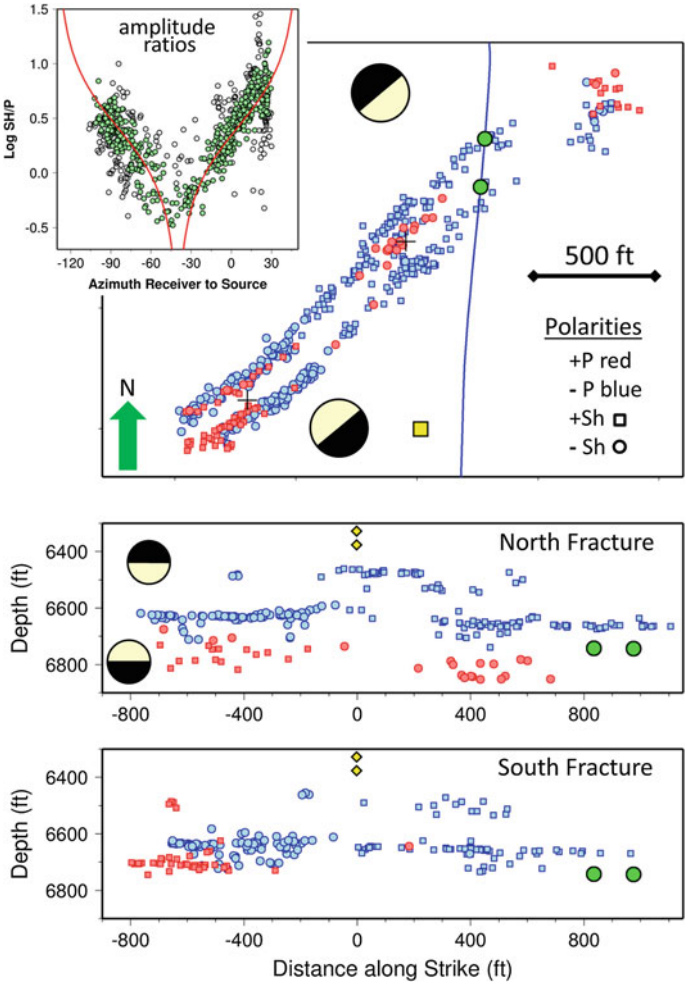

Fig. 5 High-precision microseismic source locations from one stage of a Barnett shale completion. Two mechanism families with opposite sense of first motions are distinguished by red and blue symbols. Two perforation intervals (green circles) spaced 200 ft apart were stimulated simultaneously. Two separate fractures growing from the isolated perforations intervals are resolved and are displayed separately in depth. The data were acquired on a 20-level vertical array of 3-component geophones spanning 950 ft. The monitor well is shown as the yellow square; the two deepest geophones are the yellow diamonds in the depth views. The SH- to P-wave amplitude ratios (SH/P) averaged over the array are shown with respect to the azimuth from the monitor well. The red curves correspond to the theoretical SH/P for dip-slip fault plane solutions on vertical planes striking 50°. SH/P values coloured green are within ±15° of the strike of the theoretical curve. The event P- and SH-phase polarities are distinguished by colour and symbol shape, respectively. The hemisphere projections for the P-wave first motions in depth view are towards the viewer and correspond to the red events (shown deeper) and the blue events (shallower). After Rutledge et al. (2015)

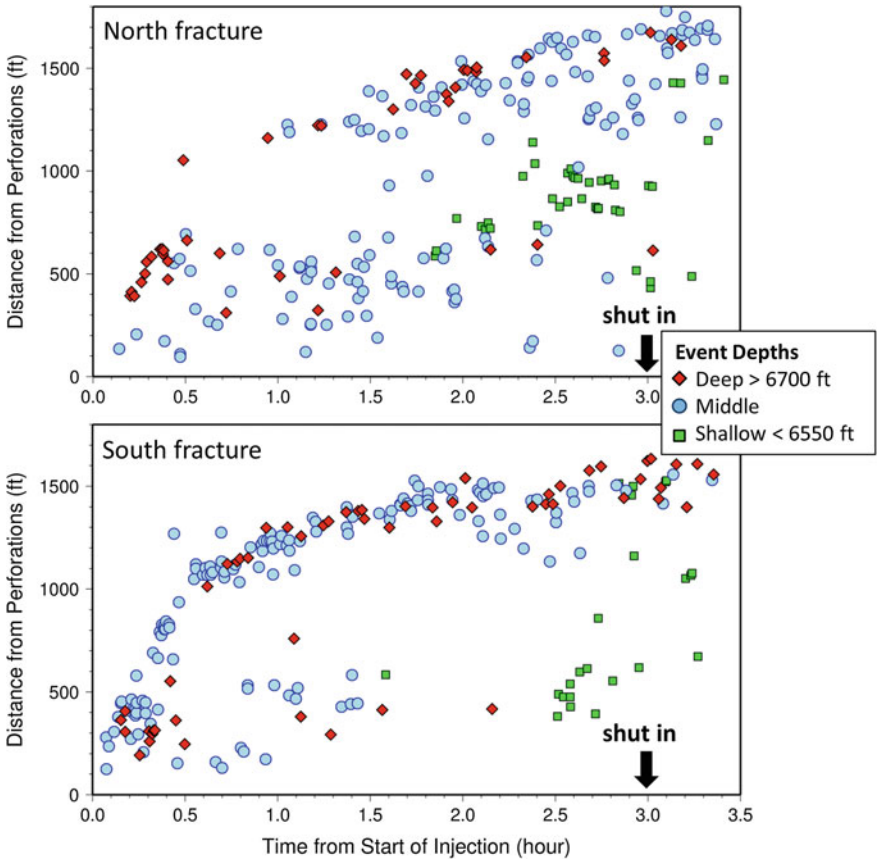

Fig. 6 Temporal development of the two separate fractures with respect to distance southwest from their respective perforation intervals for the Barnett completion shown in Fig. 5. Injection lasted 3 h at a rate of 80 bbl/min. Symbol color distinguishes three major depth intervals of events. After Rutledge et al. (2015)

shear failure driven by coupling of the hydraulic fracture pressure into the formation should often be weak.

Horizontal, or near-horizontal bedding planes are discontinuities common to most shale reservoirs. The common observation of dip-slip events in shale stimulations is probably easier to explain by considering the horizontal nodal plane as the slip plane, where the shearing occurs on weak bedding planes driven by the stresses/strains of hydraulic fracture opening. Shear at bedding planes can be driven by fracture tip stresses of a vertically-oriented extension crack approaching and interacting with the interface. The symmetry of stress changes should produce opposite senses of lateral displacements, left and right of the fracture tip (e.g., Cooke and Underwood 2001). From the time-space patterns and continuity of events and mechanisms displayed in Figs. 5 and 6, Rutledge et al. (2015) interpreted the microseismic shearing to be asso-

ciated with step-overs formed as vertical hydraulic fractures jog at bedding interfaces, where the opening of a vertical crack is translated to a critical shear displacement. The development of step-overs is also described by crack tip stresses acting near a bedding interface. As a vertically-oriented extension crack approaches the mechanical discontinuity of bedding, the maximum tensile stresses offset symmetrically from the approaching crack (Helgeson and Aydin 1991; Cooke and Underwood 2001). The propensity for the crack to step one way is often controlled by presence of natural flaws, allowing continued vertical growth to reinitiate on one of the two maxima, left or right. Rutledge et al. (2015) proposed that the opposite senses of shear observed in the Barnett case are the result of opposite senses of step created at bedding interfaces.

As noted in Rutledge et al. (2016) the step-over interpretation is problematic. Modeling studies and field observations indicate that the offset of peak stresses from the parent tensile crack and the size of step-overs associated with crack tips stresses are typically on the order of a few centimeters (Cooke and Underwood 2001; Zhang and Jeffrey 2008; Chuprakov et al. 2011). Based on common magnitude scaling relationships, and for typical monitoring geometry, downhole detection of microseismic signals is limited to source lengths of about 0.5 m and generally larger for surface monitoring where dip-slip/horizontal-slip mechanisms are also commonly observed during shale stimulations. Thus, common step-over features should be too small to produce the microseismic observation unless the shear displacement extends considerably further along bedding. Further, larger jogs, if formed, will tend to elevate fracture pressures and arrest vertical fracture growth (Zhang and Jeffrey 2008).

Slip induced on bedding does not require a step-over or fracture termination. An extension crack can arrest, weaken and shear the interface and, under certain conditions with net pressure recovery and gain, then continue propagating across the interface. Chuprakov and Prioul (2015) present a model where vertical hydraulic fracture growth is slowed or terminated by contact with relatively weak bedding interfaces. A schematic of the model is shown in Fig. 7 where the fracture tips are blunted as they simultaneously contact interfaces above and below. During crack arrest, shearing can be promoted by fluid/pressure invasion along the bedding and the horizontal stress added by the fracture net pressure. For this model to be pertinent in describing microseismic observations, the scale length of the shearing along the interfaces would have to approach source dimensions on the order of a few meters.

2.3 Interpretation

The general pattern of P-wave first motions on both the north and south fractures show dilation first motions near the base of the fracture and compressional arrivals associated with the upward growth (Fig. 5). For the proposed geometry shown in Fig. 7, and the possible symmetries of mechanisms, the observations indicate that the bedding plane slip largely occurs on the northwest side of the fractures. This preference for shear to the northwest side may be due to the stress shadow effects of five stages previously completed to the southeast. The increased horizontal stresses associated

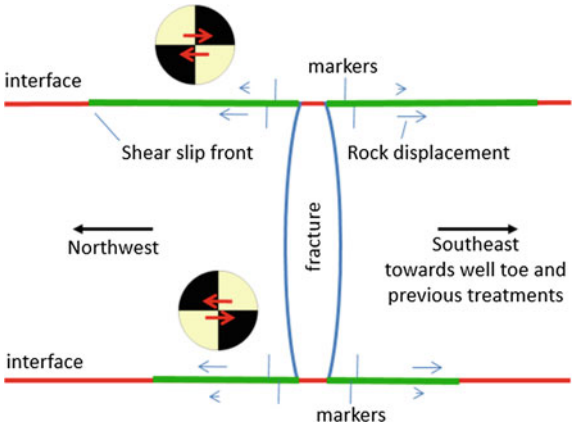

Fig. 7 Schematic of fracture arrest and shearing at bedding interface contacts. The rock displacements driven by fracture opening are shown with the blue arrows and markers. The markers would be aligned before fracturing, and here show the relative displacements of the rock on both sides of the interfaces with fracturing. Fluid invasion and pressure coupling weaken the interfaces. Opposite senses of shear would be generated both left and right of the fracture contacts, and at upper and lower interfaces. The P-wave first-motion diagrams show the relative sense of shear observed near the base of the Barnett fractures and that associated with upward growth at interfaces (Fig. 5). For this model, applying the first motion relationships observed in Fig. 5 indicates the bedding-plane shearing is preferentially occurring on the northwest side of the hydraulic fractures as highlighted by the two first-motion diagrams

with opened fractures to the southeast would tend to inhibit the induced displacements toe-ward of the treatment well and promote the shearing on the northwest side (Fig. 7). Similar symmetry in first motions of dip-slip/horizontal-slip mechanisms were observed in a series of Marcellus shale hydraulic-fracture completions, which may also be attributable to stress shadowing effects (Tan and Engelder 2016).

The general time-spatial sequence and continuity of events displayed in Figs. 5 and 6 show the shearing progressing down the horizontal structures. The effects not included in quasi-static models of interface slip would be the dynamic effects of critical shear failure and the mode III loading of the bedding surfaces ahead of the hydraulic fracture propagation direction by stress transfer. The dimensions of the shearing surfaces parallel to the fracture propagation direction may also be longer than the lengths orthogonal to the parent fracture, contributing to more detectable, larger magnitude signals. The events occurring behind the seismic front implied by Fig. 6 also indicate that bedding-plane slip can continue or repeat after the fracture tip propagates away from the active bedding surfaces.

The vertical development of the fractures appears to be more inhibited downward with the red events of Fig. 5 defining a dispersed lower boundary. The middle band of events near 6600 ft depth appear to define a clear bedding boundary where the fracture's upward growth may temporarily halt. But the eventual appearance of the

top band of events indicates the upward growth continues through the mid-depth, seismically active interface.

3 Characterization of a Laboratory-Scale Hydraulic Stimulation Through the Moment Tensors of Acoustic Emissions

Laboratory experiments offer a controlled environment where one can gain insight into the mechanics of hydraulic stimulations. As with other smaller-scale simulations of earth phenomena, the main limitation of the understanding obtained from laboratory experiments is the extrapolation of results and interpretations to field-scale. Having that in mind, laboratory experiments are still an important tool in the study of hydraulic stimulations. In this section, we illustrate the last statement with the analysis of the MTs of acoustic emissions (AEs) observed during the hydraulic stimulation of a sandstone block under triaxial stress conditions.

AEs are seismic events that obey the same physics of elastodynamics. The name AE is used in fields such as geotechnics (Koerner et al. 1981; Hardy 2003), where the analysis is often focused upon compressional wave arrivals. For the experimental data considered in this section, we were able to isolate both direct P and Sv arrivals from the recordings. Therefore, the MTs described in the following paragraphs come from the fitting of both wave phases.

3.1 Description of the Experiment

The rock sample used was a Colton sandstone block. The dimensions of the block and other details of the experimental setup can be obtained from Table 1, Fig. 8 and Vera Rodriguez et al. (2017). The block was instrumented with 38 one-component, piezoelectric transducers distributed over its six surfaces. The monitoring array offered a coverage of the focal sphere never available, to the extent of our knowledge, in field-scale hydraulic stimulations. Further details regarding the acquisition system and characterization of the transfer function of the sensors can also be found in Vera Rodriguez et al. (2017). As part of the preparation of the block, vertical slots were sandblasted in the open hole section of the borehole to promote initiation of hydraulic fracturing in the direction of maximum horizontal stress. Before the start of the experiment, the block could be described as homogeneous in its fabric, without visible layering or noticeable pre-existing fracturing.

Once the block was subjected to the desired state of stress, the injection fluid of 2.5e6 cP viscosity was pumped at a rate of 5 mL/min until a few seconds after the breakdown point was detected in the borehole pressure measurements. The breakdown corresponds to the point in time when the maximum borehole pressure is

Table 1 Completion details of the experiment

Rock type	Colton sandstone
Dimensions (mm)	$228.6 \times 279.4 \times 381.0$
Borehole diameter (mm)	25.4
Borehole depth (mm)	228.6
Cased hole section (mm)	165.1
Open hole section (mm)	50.8
Epoxy plug (mm)	12.7
Fracturing fluid	Silicon oil
Fluid viscosity (cP)	2.5e6
Injection rate (mL/min)	5
Vertical stress (σ_1) MPa	27.6
North-South stress (σ_2) MPa	13.8
East-West stress (σ_3) MPa	6.9

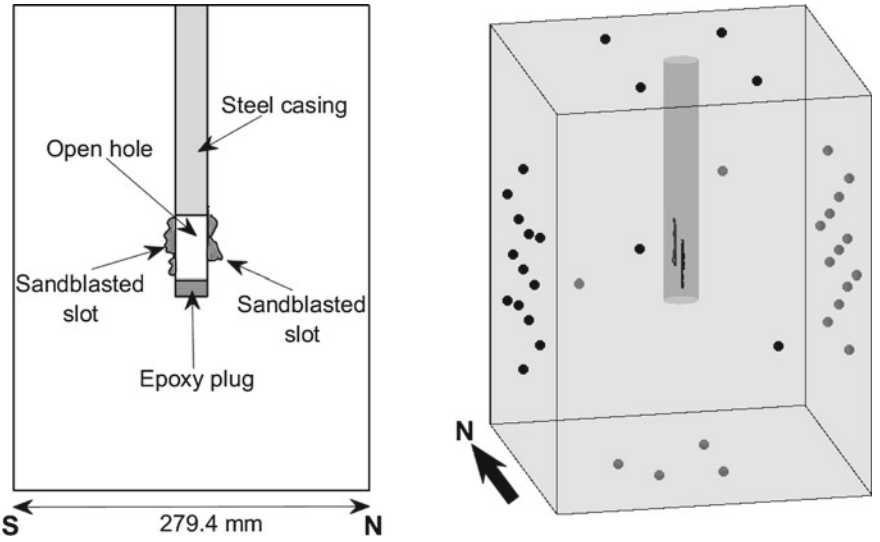

Fig. 8 Left: schematic diagram showing the completion details of the block and the approximate geometry of the sandblasted slots (as observed after the experiment over the open block). Right: distribution of receivers (black and grey dots) over the block boundaries

recorded. After the injection was stopped, the pumps were reversed to withdraw fluid from the borehole at a rate of 1000 mL/min. The objective was to stop the propagation of the hydraulic fracture before it reached the boundaries of the block. During the entire experiment, the stresses at the boundaries were controlled to be constant. After the block was removed from the presses, it was split in two along the surface of the created hydraulic fracture (Fig. 9).

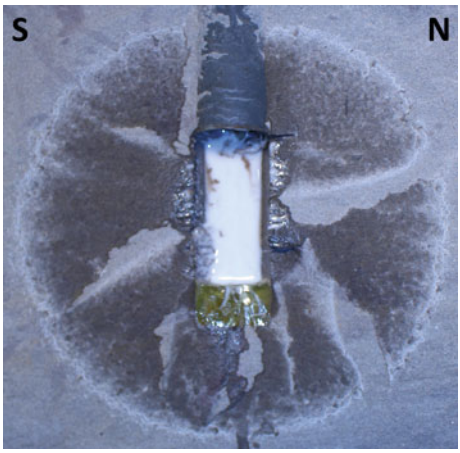

Fig. 9 Fracture plane observed after the block was split in two. The stripes displaying lighter colour correspond to regions of the fracture plane that were not invaded by the injection fluid. These are later referred to in the text as "dry stripes"

In total, 15,756 AEs were extracted from the monitoring records. To estimate their locations, a velocity model was constructed using measurements of compressional speed along ray paths connecting different pairs of transducers. For this purpose, the transducers were activated as ultrasonic transmitters one at a time while the rest of the array was listening. These measurements were taken at the start of the experiment with the block already compressed at the desired state of stress. The average shear wave velocity for the block was derived by matching the geometry of the cloud of located AEs to the surface of the fracture measured over the open block. The frequency spectra of all the AEs was also filtered to the range 90–200 kHz so the data would correspond to the far-field for the MTI. Additionally, the recordings were corrected for instrument response, coupling effects and the angular sensitivity of the receivers. Vera Rodriguez et al. (2017) present a detailed description of the processing workflow to obtain the MT solutions in this dataset.

More recently, we have conducted an analysis of the evolution of the attenuation properties of the block along the three coordinate directions and over time. From the results of this analysis, the recordings have been corrected for attenuation and new MT solutions have been estimated. The MTs presented in the following subsection correspond to our latest results incorporating spatio-temporally varying attenuation corrections.

3.2 Analysis of the Estimated Moment Tensors

The most reliable MT solutions were selected taking into account the following criteria: distance from the AE to each receiver (>50 mm to meet the far-field assumption), normalized misfit of the solution with the observations (<0.3, except for the interval 0–2300 s where we used <0.36), and the sensitivity of the MTI to random noise per-

turbations (measured as the dispersion of multiple, noise-perturbed inversions over a Hudson's plot <0.05). Using all of the above elements, the number of solutions left for analysis was reduced to 4,788. MTs were also decomposed, using the biaxial decomposition (Chapman and Leaney 2012), into general dislocations represented by the angles of strike, dip, rake, and deviation from pure shearing or α (Vavryčuk 2011; Chapman and Leaney 2012). Each MT can be associated with two different dislocations due to the ambiguity between the displacement vector and the normal to the dislocation plane. In every case, the dislocation with the largest dipping plane was categorized into one family of solutions and the remaining dislocation into a second family. Afterwards, we retained only those dislocations that could be associated with a stress regime. For example, normal faulting (negative rake or extensional stress regime) was linked to opening dislocations ($\alpha > 10°$). Similarly, reverse faulting (positive rake or compressional stress regime) was linked to closing dislocations ($\alpha < -10°$). Shear dislocations were accepted in all cases ($|\alpha| < 10°$). The cut-off angle of 10° is arbitrary but takes into consideration the uncertainty carried on from the MTI onto the decomposed dislocation angles. While in some instances this selection process allowed only one dislocation to be associated with an AE, in many cases, both dislocations were consistent with a stress regime and were retained. In the following, the source mechanisms are analysed focusing on their evolution during the experiment, for which we will present groups of AEs observed in progressive time intervals.

The first part of the experiment corresponds to the AE activity observed before the initiation of the hydraulic fracture (0–2300 s, Fig. 10). The initiation point is identified as an increase in the number of detected AEs and the deformation of the block in the direction of minimum stress (Zoback et al. 1977). The AE activity takes place north and south of the borehole (Fig. 11). The AEs located in the south appear next to the sandblasted slot and present predominantly opening components under 30°. These dislocations seem directly connected to the borehole; therefore, they are being consistently activated by the tensile push of the injection fluid. The initiation of the fracture could have started earlier on this side of the borehole. The AEs displayed in the north side took place farther away from the sandblasted slot and show a mix of low-angle opening and closing source mechanisms. If we added the locations of AEs for which MT solutions were discarded, we could see that these AEs could be connected to the borehole from its intersection with the sandblasted slot. In particular, the high-magnitude, closing event near the bottom, could be associated with the activation of a pre-existing crack, likely linked to the deformation (compression) of the block. During this part of the experiment, the fluid could not leak-off into the rock due to its high viscosity; therefore, the block was being internally compressed by the increase in fluid volume and pressure build up inside the borehole. Given the distribution of the principal stresses imposed over the outer boundaries (see Table 1), there is a preferential activation of highly dipping dislocations aligned closer to the north-south direction.

After initiation, the opening fracture can start accepting fluid depending on its width and the viscosity of the fluid. Lower viscosity fluids can flow more easily towards the opening fracture. In the case of our experiment, however, the high vis-

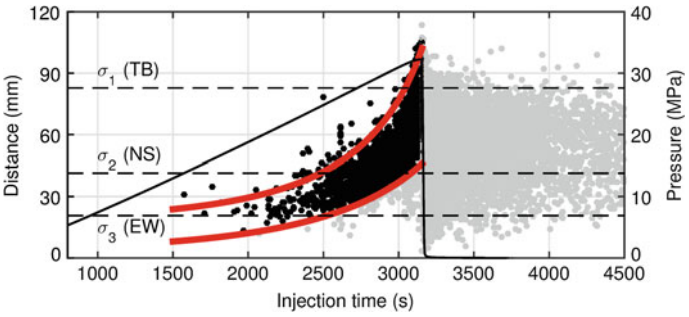

Fig. 10 AE distance from the injection point along the fracture plane. AEs between the two thick red lines (black dots) are interpreted to have taken place near the edge of the propagating fracture. The rest of the AEs (grey dots) are interpreted to have taken place at the back of the fracture's edge. The black solid line is the borehole pressure; the steep fall of this curve marks the moment when the pumps were reversed to withdraw fluid

cosity of the injection fluid resulted in a period of time during which the fracture propagated dry (Stanchits et al. 2015). Figure 12 shows a set of AEs observed at the start of this period of dry propagation. The orientation of the dislocations are now better defined close to the north-south direction with highly dipping angles.

The style of activation is also dominated by dip-slip components. The main fracture plane appears already well-defined in the south side of the borehole, while in the north side there is still activity in front but also growing from the sandblasted slot. It appears that the block had a network of weakness planes (e.g., micro-fractures) in this area that influenced the initial development of the north side of the main fracture plane. Most AEs reflect opening dislocations at angles predominantly under 30°. Up to this point there is no evidence of fracture growth below the bottom part of the borehole.

Non-opening events are observed in some cases separated from the main AE cluster. When inside the main cluster, non-opening events can often be associated with regions where the fracture found barriers restricting its growth (Fig. 13, bottom row). These regions are identified in the open block as dry stripes. We can also see an absence of opening events inside these stripes during some time intervals (e.g., Fig. 13, intervals 2650–2800 s and 2950–3010 s), and that some of the lower-angle opening AEs fall in their surroundings. We speculate that non-opening AEs that cannot be associated with dry zones in the open block could also correspond to regions where fracture propagation was initially restricted, but that were finally opened during the experiment, sometimes enough to permit fluid invasion. According to this interpretation, the lower part of the fracture plane was the most difficult to develop, since it contains a significant proportion of non-opening events, and also because multiple dry stripes can be observed in the open block. The north and south sides also display concentrations of non-opening events near dry stripes. Restrictions to fracture growth can be the result of variations in the rock strength,

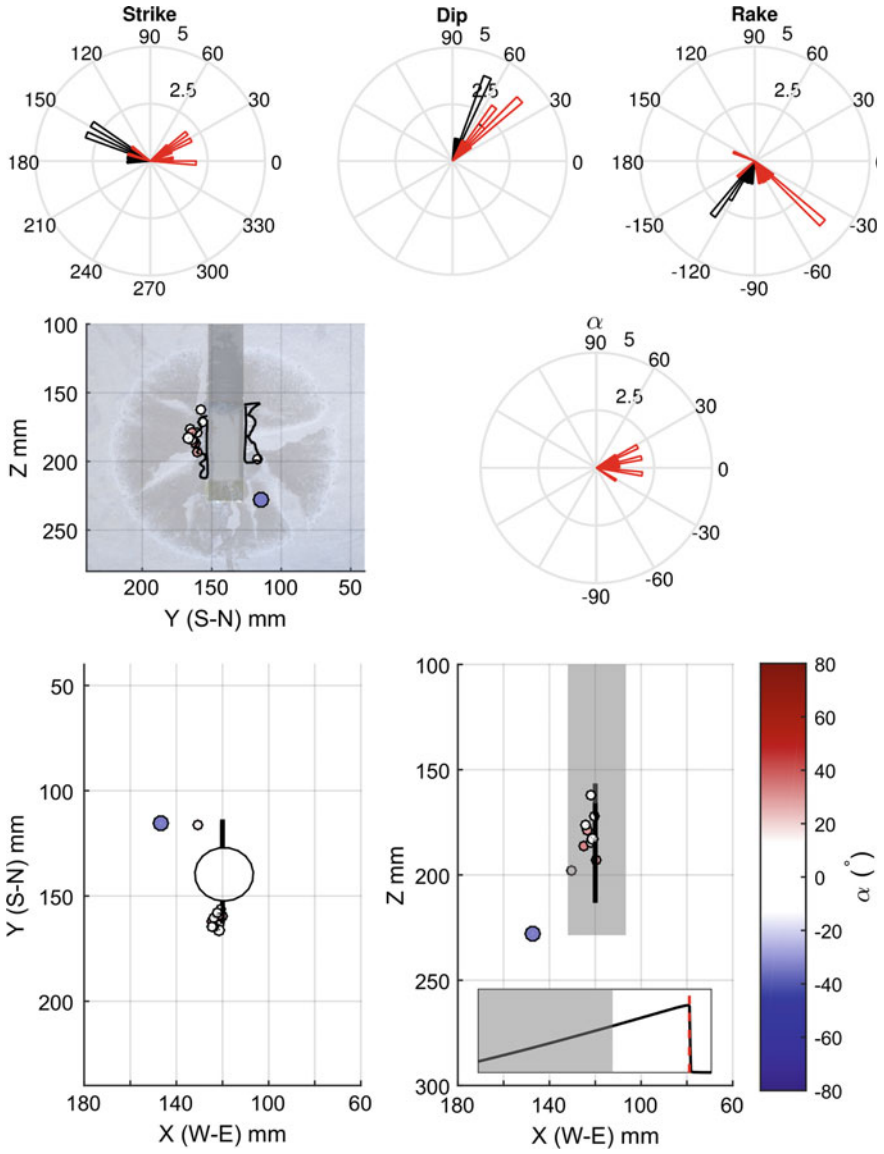

Fig. 11 Source mechanisms of AEs observed during the interval 0–2300 s. Black and red colours on the rose plots correspond to the two families of dislocations extracted from the AE MTs. Dots represent AEs coloured by their angle of deviation from the DC source (α) and sized by their relative magnitude. The picture of the actual fracture plane is also showed as a reference in the background of the front-view plot. Black-solid lines follow the approximate contour of the sandblasted slots. The inset plot displays the position of the time interval (grey rectangle) with respect to the borehole pressure (black line) and the breakdown point (red, vertical-dashed line)

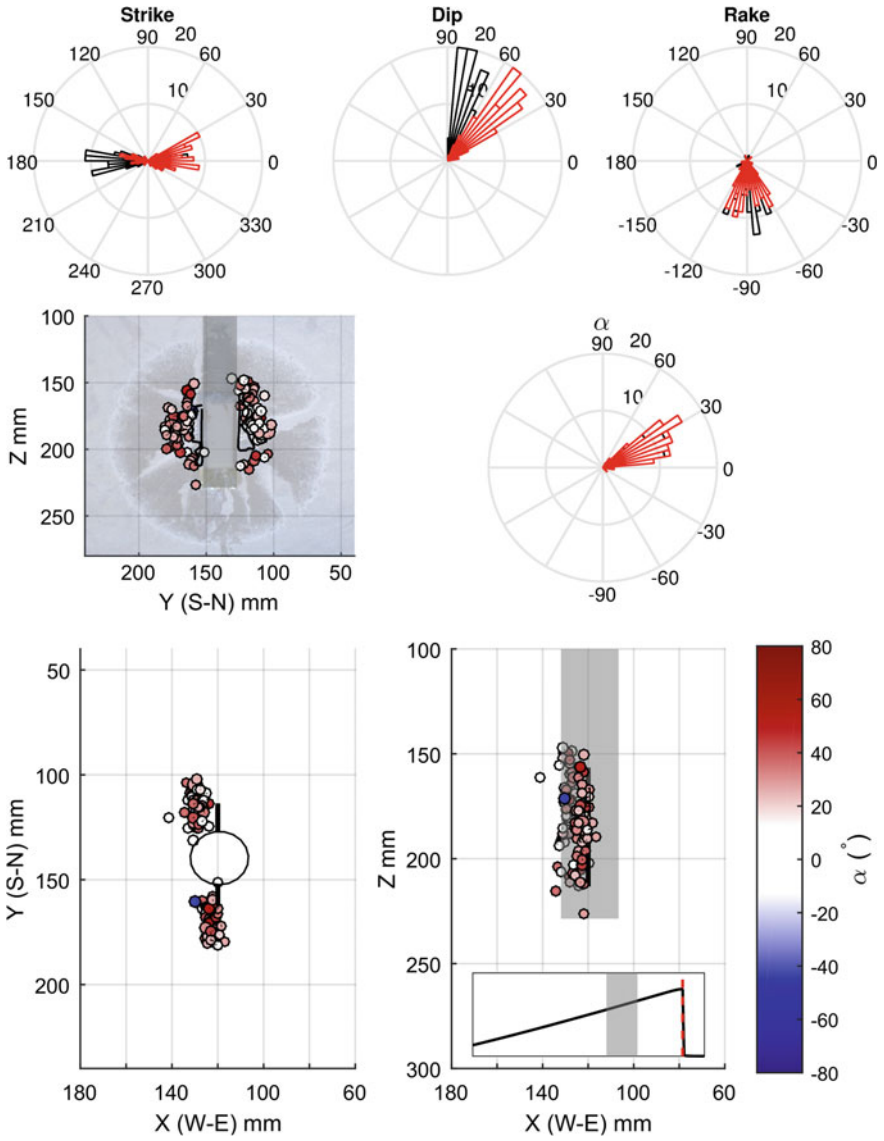

Fig. 12 As Fig. 11 except time interval is 2300–2650 s

fabric, distribution of stresses around the borehole and/or a combination of all these factors.

In experiments with low viscosity fluids, fracture initiation can coincide with breakdown, i.e., when the elastic energy stored in the system is suddenly released after the borehole pressure reaches its peak value (Zoback et al. 1977). With increasing

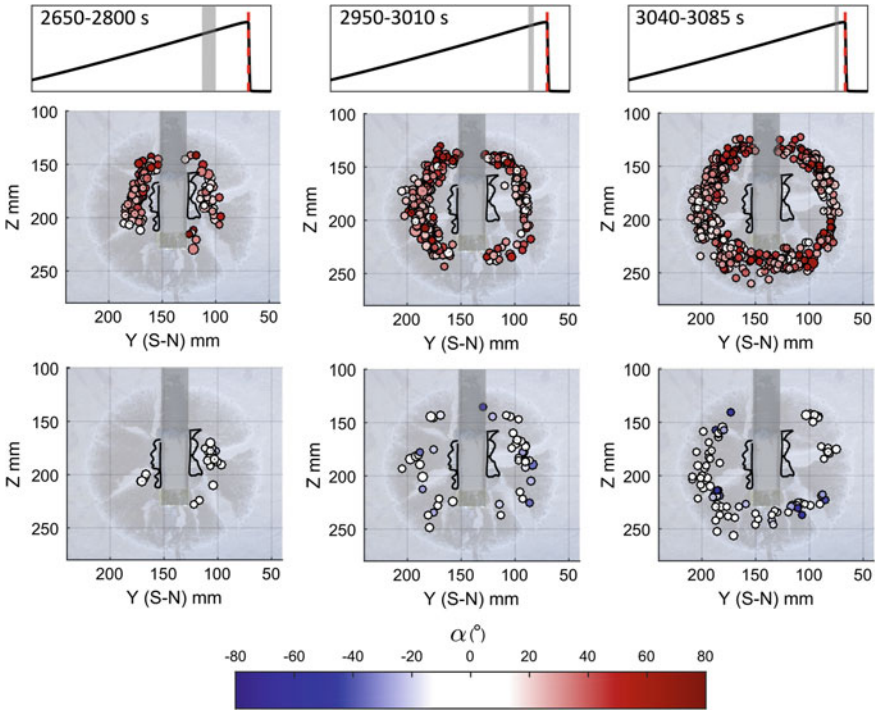

Fig. 13 AEs observed in successive time intervals during the dry fracture propagation stage. Top row are opening AEs ($\alpha > 10°$). Bottom row are shearing ($|\alpha| < 10°$) and closing ($\alpha < -10°$) AEs. The plots at the top display the position of the corresponding time intervals (grey rectangles) with respect to the borehole pressure (black line) and the breakdown point (red, vertical-dashed line)

fluid viscosity, fracture initiation takes place in advance of breakdown, introducing a period of controlled fracture growth. As mentioned before, part of this controlled growth can take place with fluid entering the fracture depending on fracture width and fluid viscosity. In our experiment, a period of lubricated fracture propagation is identified starting with a slowdown in the rate of increase of the borehole pressure (onset of leak-off towards the fracture) until the point where it reaches its maximum value at breakdown. This corresponds to the time interval from 3085 to 3155 s (see Fig. 10). Most of the fracture growth took place during the dry fracture propagation period as a result of the pressure build up at the borehole. With the flow of the fluid towards the fracture plane, this pressure build up was relaxed, which in turn slowed down fracture growth until it was finally stopped by the reversal of the pumps to withdraw fluid from the borehole (Fig. 14, left). The source mechanisms remain consistent during this period of fracture growth, with mainly sub-vertical dislocation planes aligned near a north-south orientation and being activated in a predominantly dip-slip direction with opening angles around 30°. Only a slight increase in the

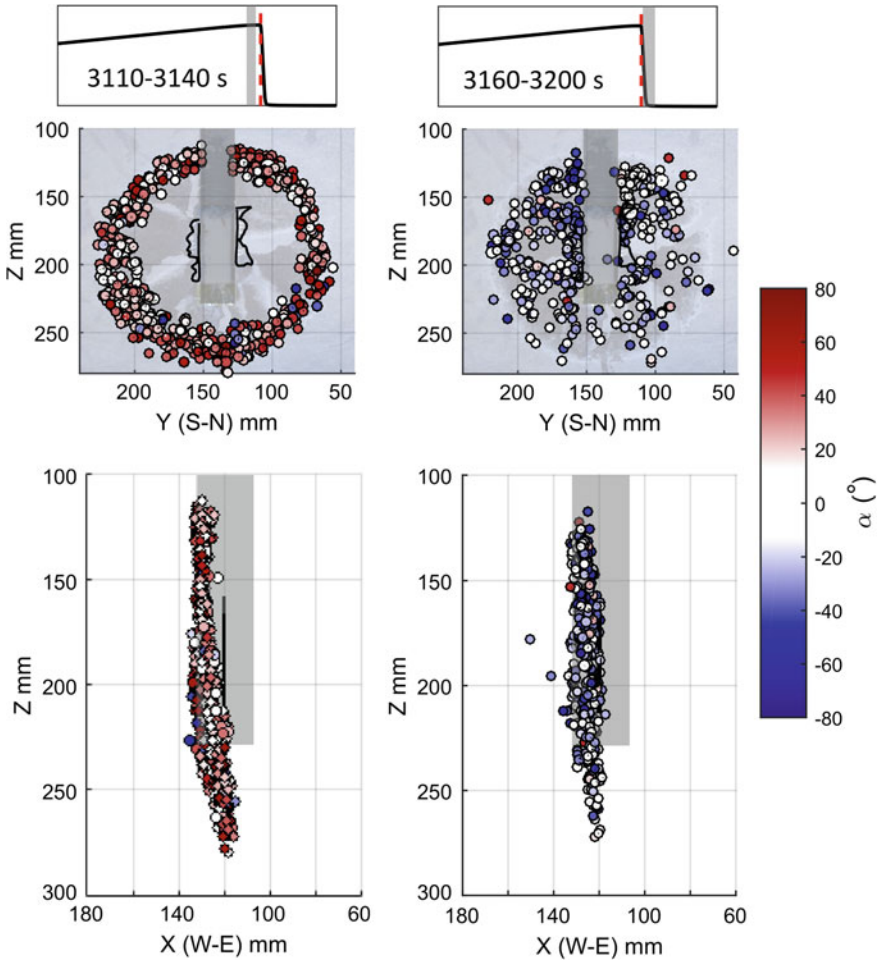

Fig. 14 AEs observed during two time intervals corresponding to the lubricated fracture propagation (left) and closing (right) periods of the experiment. The plots at the top display the position of the corresponding time intervals (grey rectangles) with respect to the borehole pressure (black line) and the breakdown point (red, vertical-dashed line)

dispersion of the dislocation angles with respect to the aforementioned directions of alignment could be observed.

With the reversing of the pumps to withdraw fluid from the borehole, the whole fracture plane started closing. This is reflected both by the locations and the source mechanisms of the AEs observed during this period of time (Fig. 14, right). Generally speaking, the amount of deviation of closing AEs from the DC case is smaller than in the case of opening AEs. Also, the maximum deviations from DC occur at the beginning of the closing period and reduce towards the end of the experiment. In other

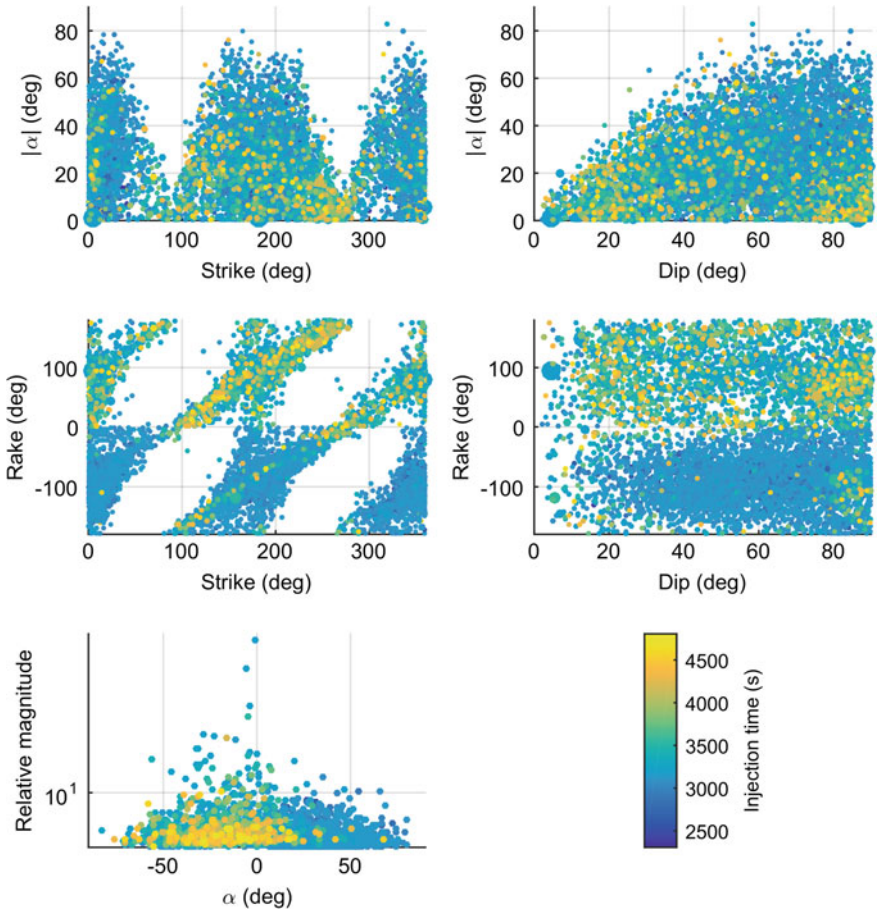

Fig. 15 Scatter plots between different dislocation angles and between the angle α and the relative size of the AEs. Only combinations that displayed some sort of correlation are presented. Both dislocation families, after filtering for stress regime consistency, are included in the plots

words, most of the last-observed AEs are predominantly of shearing type. Closing AEs are better explained by the collapse of asperities holding sections of the fracture open while the injection fluid was being withdrawn. Otherwise, the closing of flat dislocation surfaces would require a fast squeezing of the injection fluid, which is more difficult to support given its high viscosity.

Looking at correlations between dislocation angles during the complete duration of the experiment (Fig. 15) we can make the following observations:

- Dislocation planes lying parallel to the main fracture plane (north-south) present the largest components of opening/closing. As the strike of the dislocation deviates from the north-south direction towards the east-west direction the amount of permissible opening/closing is reduced, so the events are predominantly shearing. The same effect is observed when the dip of the dislocation reduces towards the horizontal plane.
- The maximum deviation from pure shearing is reached for dislocations dipping around 60°, this is 30° from the direction of the maximum principal stress. Above this dip angle, the maximum deviation from pure shearing remains stable around $|\alpha| \sim 70°$.
- Dislocation planes lying parallel to the main fracture plane (north-south) are activated predominantly in dip-slip but their activation can also take place in practically any other direction from dip-slip to strike-slip. As the dislocation-plane strike deviates from the north-south direction towards the east-west direction, the activation mode becomes restricted towards strike-slip only.
- Opening AEs during the first part of the experiment (fracture propagation) are predominantly activated near dip-slip directions. Closing AEs during the second part of the experiment (fracture closure) show more deviations from dip-slip toward strike-slip activation.
- Relative AE magnitude reduces quickly for $|\alpha| > 50°$. AEs that are closer to the pure DC case display the largest relative magnitudes.

Shearing AEs

Shearing AEs (i.e., AEs with $|\alpha| < 10°$) account for 19% of the total number of MTs selected for analysis. If we assume that the criteria used for selection are independent of the angle α, we can consider this number is also representative of the general distribution of AE source mechanisms (α is unique for each AE). In a similar way, we estimate that shearing AEs account for 19% of the total seismic moment released during the experiment. The events with the larger individual magnitudes in the catalogue are also of shearing nature with dip-slip style of activation. The contribution from shearing AEs to the total number of observed events increased during the experiment from 11% during the dry fracture propagation period, to 17% during lubricated fracture propagation, and finally to 27% during the closing of the fracture. We speculate that the percentage of shearing AEs during the closing stage would have been larger if the pumps had not been reversed to control the growth of the fracture.

In field-scale hydraulic stimulations it is common to observe increases in the number of detected microseismic events after falls in borehole pressure. Similarly, source mechanisms derived from surface monitoring arrays (which usually provide better focal coverage compared to downhole monitoring arrays) tend to describe predominantly shearing events. Normally, only the events with higher signal-to-noise ratio are selected for MTI in field-scale applications. The results from this experiment suggest that, considering relative magnitudes, shearing events could be more likely to be detected and selected for MTI than opening and closing events in field-scale microseismic monitoring. The increase in shear activity observed during

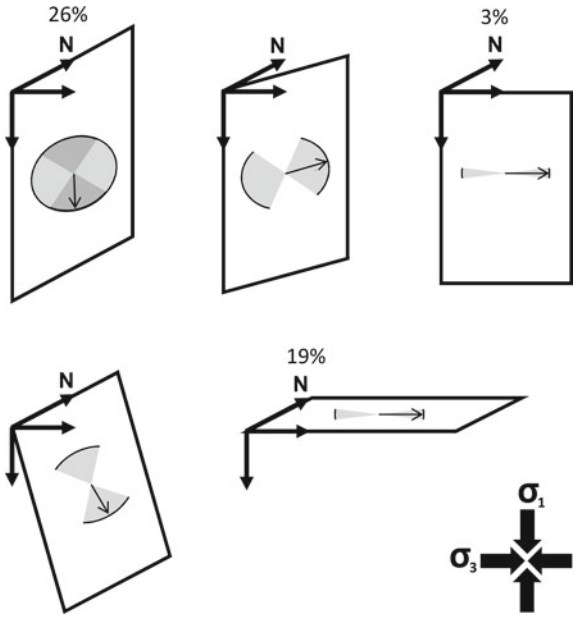

Fig. 16 Representation of the ranges of activation constrained by the orientation of the dislocation plane with respect to the stress field. The black arrow represents the direction of slip and the grey areas the permissible activation ranges. The darker areas in the top-left image denote that although activation can take place in all directions, dip-slip is dominant. The numbers are percentages (with respect to shear-only AEs) observed during the complete experiment. These percentages include both dislocation solutions from the MT decomposition

the closing stage of the experiment is also consistent with this hypothesis and the increase in microseismic event detections during pressure drops at field-scale.

The geometry of individual dislocations is controlled by the rock's strength and fabric, and the local state of stress. Similarly, the style of activation is constrained by the orientation of the dislocation plane with respect to the stress field. For instance, for dislocation planes aligned with the stress field (i.e., parallel to the main fracture plane) the rake or direction of slip can vary from dip-slip to strike-slip style of activation (although dip-slip is significantly dominant). Changing the strike while maintaining the dip constant near 90° reduces the range of permitted activation style towards strike-slip. On the other hand, changing the dip while maintaining the strike aligned with the main fracture plane reduces the range of activation style towards dip-slip. In both cases, the slip direction is constrained towards alignment with the direction of minimum principal stress (Fig. 16).

In this analysis of shear sources we have considered the two dislocation planes that are obtained from the decomposition of each MT. Additionally, we did not remove shear AEs with activation styles that contradicted the main stress conditions at a particular time during the experiment. For example, during fracture opening we retained shear sources denoting reverse faulting, and vice versa during the closing stage. These criteria accept the possibility of local variations in the stress field that include reversals. Further geomechanical modelling of the fracturing experiment is necessary to validate or discard this possibility.

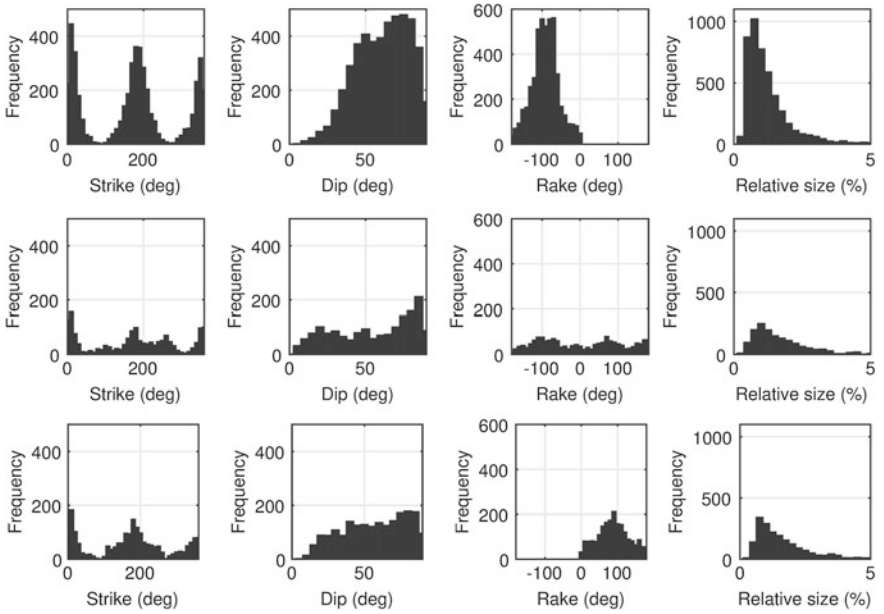

Fig. 17 Distribution of dislocation angles for opening (top), shearing (middle) and closing (bottom) AEs. Both dislocation solutions are represented in the histograms after filtering by consistency with stress regimes. Relative sizes are estimated with respect to the AE with the largest seismic moment in the complete catalogue, a dip-slip shear event

3.2.1 Opening AEs

Opening events are favoured by high viscosity injection fluids (Matsunaga et al. 1993; Bennour et al. 2015). In consequence, it is possible that with a lower viscosity injection fluid, the maximum AE opening angle observed in our dataset could have been smaller, and/or the frequency of opening AEs could have been less. Opening dislocations account for 52% of the catalogue of AEs. Their contribution in number decreases from 85% of the total during the dry opening period, to 74% during lubricated propagation, and down to 10% during the closing of the fracture. The seismic moment released from opening AEs corresponds to approximately 52% of the total during the complete duration of the experiment, most of it released during the opening stages. The largest magnitude opening event took place soon after the start of the fracture closure period. It was located near the border of a dry stripe on the north side of the fracture with $\alpha = 49°$. It is almost half the size of the largest shearing event and about 75% the size of the largest closing event. Most opening AEs are about 0.75% the size of the largest shearing event (Fig. 17, top). This is not too far from the 1% mode observed in the distribution of relative sizes of shearing events (Fig. 17, middle). The decay in the distribution of relative magnitudes is steeper for opening than for shearing AEs towards bigger-sized events.

The rake of opening AEs is also controlled by the orientation of the dislocation plane within the stress field (see Fig. 16). Opening is favoured in dislocation planes that strike in the direction of the main fracture plane and dip at intermediate-to-high angles (Fig. 17, top). On the other hand, opening is limited by the action of the maximum and intermediate principal stresses; therefore, there are virtually no opening dislocations with planes near the horizontal or aligned in the east-west direction. The style of activation concentrates towards dip-slip, normal faulting but, as mentioned above, rake can also deviate toward strike-slip when the dislocation plane is aligned with the main fracture plane.

3.2.2 Closing AEs

Closing AEs represent 29% of the total number of events in the catalogue. Their number increases from 4% during dry fracture propagation, to 9% during lubricated fracture propagation, and finally to 63% during fracture closure. In terms of seismic moment release, closing AEs account for 29% of the total. The largest closing event is about 60% the size of the largest shearing event, with the histogram of relative sizes behaving similarly to that of shearing events in its decay but with a mode at 0.75% as in the case of opening events (Fig. 17, bottom).

For a fluid-filled dislocation, closing accompanied by seismic energy release requires a fast compression and/or retreat of the fluid inside. The block was not artificially dried or saturated for the experiment; therefore, it contained a mix of interstitial fluids and air filling its pores. Closing AEs outside the fracture plane and before breakdown can be explained by the collapse of cracks in response to the compressive deformation of the block produced by the opening fracture. Cracks filled with air and/or connected to high permeability paths would be more likely to release seismic energy. Closing AEs located inside the fracture plane during the same period of time seem related to regions where fracture propagation was limited by the rock's strength and fabric. For AEs located within the fracture plane during closing, the low compressibility and high viscosity of the fluid used in the experiment makes the release of seismic energy while closing improbable without the external help of the pumps. Therefore, it is possible that a significant amount of closing AEs were the result of the reversal of the pumps producing sudden drops in pore pressure along high permeability paths across the fracture plane. The presence of asperities over the fracture plane could prevent a smooth closing as the pore pressure dropped, resulting in negative pressure build up and eventual, sudden collapses along the asperities. It is also possible that in the absence of the fluid withdrawal process, fewer closing and more shearing AEs could have been observed.

The distribution of dislocation geometries of closing AEs is similar to that of opening AEs, with the increase in intermediate-dipping planes not observed in shearing AEs (Fig. 17). The only noticeable difference is an increase in the proportion of dislocations dipping under 50° compared to opening AEs. The dislocation planes are also preferentially oriented in the north-south direction, although the decrease in the number of dislocation planes oriented in the east-west direction is not as smooth

as with opening AEs. The activation of closing dislocations follows also a preferential dip-slip direction, although there is a higher proportion of deviations towards strike-slip compared to opening AEs.

4 Conclusions

The examples presented in this chapter illustrate the usefulness of MTs for the understanding of the mechanics of hydraulic stimulations both at different scales and in different lithologies. Furthermore, the examples highlight the benefits of incorporating additional, independent sources of information for the interpretation of dislocation planes extracted from MT solutions. For instance, in the field case study, we proposed that the observed microseismicity is generated by bedding-plane slip using a model where vertical fracture growth is halted or slowed at bedding interfaces. The general patterns of first motions observed on two distinct, parallel fractures propagating simultaneously suggest that events detected near the base of the fracture and those associated with upward growth tend to occur preferentially on the heelward side of the treatment well and away from the direction of previously completed hydraulic-fracture stages. We propose that stress-shadow effects with increased horizontal stresses generated southeastward by previously completed stages in the treatment well break the expected symmetry of opposite shearing left and right of the fracture contact at an interface, where the elevated stress inhibits displacements towards previously completed stages and further promotes the stress changes for bedding-plane towards the northwest.

The scale of the laboratory experiment permitted the recovery of a more complete catalogue of AEs, where the MTs describe general source types that correlate with the stress regime throughout the hydraulic stimulation process. On the other hand, the source types that are inconsistent can be associated to local effects modifying the general stress regime. For example, closing events inside the fracture plane observed during fracture opening could be linked to regions where fracture propagation was facing barriers; and those outside the fracture plane to the collapse of pre-existing cracks. Shear events and low-angle opening events could also be associated with regions of restricted fracture propagation over the fracture plane. Opening events during fracture closing were possibly the result of the injection fluid being drawn towards the borehole through regions of the fracture plane that had already closed. Notice that, despite the differences in scale and lithology, the laboratory data coincide with the field-scale example by ascribing at least part of shear activated AEs to some form of restriction to fracture growth.

In the laboratory experiment, the MT solutions describe a fracture plane that is not smooth, but rather the connection of small dislocation planes dipping at angles mostly above 30° with two possible distribution peaks, one around 45° and the other around 80°. The planes that are better aligned with the principal stresses (north-south, vertical) are those that can potentially open the most. As the planes deviate from this alignment, the action of the intermediate and maximum stress limits the maximum

opening that a dislocation can experience. The direction of slip along the dislocation plane is also influenced by the principal stresses, with the slip being aligned toward the direction of the minimum principal stress as the dislocation plane deviates from the north-south, vertical case. As the dislocation plane aligns toward the horizontal plane, with strike defined near the maximum horizontal stress, the direction of slip is restricted toward dip-slip motion, which is also consistent with the observations from the field-scale example.

The results from the experiment can also be connected to other general observations in field-scale hydraulic stimulations. For instance, the larger number of event detections observed at field-scale after pressure drops and their shear nature is consistent with the larger relative magnitudes of shear events observed during the laboratory experiment and their increase in number after breakdown. In other words, the smaller number of publications reporting opening events (compared to shear events) in field-scale stimulations might be in part a consequence of a detectability limit issue. It has to be pointed out as well, however, that the very high viscosity of the injection fluid in the experiment likely promoted more opening AEs than might be expected in field-scale operations. The large number of closing events observed in our dataset during closure might also be a particular behaviour produced by the experimental procedure. Nevertheless, a similar increase in closing source types could be expected at least during flow-back periods in field-scale stimulations.

Acknowledgements The authors would like to thank Phil Christie, Chris Chapman, Gwenola Michaud and Michael Williams for useful comments that helped improve the presentation of this chapter. We are also grateful to Devon Energy Corporation for granting permission to publish the Barnett data results and Schlumberger for permission for the publication of the laboratory data.

References

Aker E, Kuhn D, Vavryčuk V, Soldal M, Oye V (2014) Experimental investigation of acoustic emissions and their moment tensors in rock failure. Int J Rock Mech Min Sci 70:286–295

Aki K (1966) Generation and propagation of G waves from the Niigata earthquake of June 16, 1964. Part 2. Estimation of earthquake moment, released energy, and stress-strain drop from the G wave spectrum. Bull EarthQ Res Inst 44:73–88

Bennett L, Le Calvez J, Sarver D, Tanner K, Birk W, Waters G, Drew J, Michaud G, Primiero P, Eisner L, Jones R, Leslie D, Williams M, Govenlock J, Klem R, Tezuka K (2005) The source for hydraulic fracture characterization. Oilfield Rev 17:42–57

Bennour Z, Ishida T, Nagaya Y, Chen Y, Nara Y, Chen Q, Sekine K, Nagano Y (2015) Crack extension in hydraulic fracturing of shale cores using viscous oil, water, and liquid carbon dioxide. Rock Mech Rock Eng 48:1463–1473

Brune J (1970) Tectonic stress and the spectra of seismic shear waves from earthquakes. J Geophys Res 75:4997–5009

Chapman C, Leaney S (2012) A new moment-tensor decomposition for seismic events in anisotropic media. Geophys J Int 188:343–370

Chuprakov D, Prioul R (2015) Hydraulic fracture height containment by weak horizontal interfaces. Paper presented at the SPE hydraulic fracture technology conference, The Woodlands, 3–5 Feb 2015

Chuprakov D, Akulich A, Siebrits E, Thiercelin M (2011) Hydraulic-fracture propagation in a naturally fractured reservoir. SPE Prod Oper 26:88–97
Cipolla C, Warpinski N, Mayerhofer M, Lolon E, Vincent M (2008) The relationship between fracture complexity, reservoir properties, and fracture treatment design. Paper presented at the SPE annual technical conference and exhibition, Denver, 21–24 Sept 2008
Cipolla C, Wright C (2002) Diagnostic techniques to understand hydraulic fracturing: what? why? and how? SPE Prod Facil 17:23–35
Cooke M, Underwood C (2001) Fracture termination and step-over at bedding interfaces due to frictional slip and interface opening. J Struct Geol 23:223–238
Department of Energy and Climate Change (2014) Fracking UK shale: understanding earthquake risk. http://m.northyorks.gov.uk/CHttpHandler.ashx?id=32806&p=0. Accessed 19 Jun 2017
Diller D, Shuck T, Fish B (2015) Estimation and interpretation of high-confidence microseismic source mechanisms. Lead Edge 34:918–924
Duncan P, Eisner L (2010) Reservoir characterization using surface microseismic monitoring. Geophysics 75:75A139–75A146
Economides M, Nolte K (eds) (2003) Reservoir stimulation. Wiley, New Jersey
Fink J (2013) Hydraulic fracturing chemicals and fluids technology. Gulf Publishing Company, Oxford
Goertz-Allmann B, Goertz A, Wiemer S (2011) Stress drop variations of induced earthquakes at the Basel geothermal site. Geophys Res Lett 38:L09308
Hardy H (2003) Acoustic emission microseismic activity, volume 1: principles, techniques and geotechnical applications. Taylor & Francis, Lisse
Helgeson D, Aydin A (1991) Characteristics of joint propagation across layer interfaces in sedimentary rocks. J Struct Geol 13:897–911
Koerner R, McCabe W, Lord A (1981) Overview of acoustic emission monitoring of rock structures. Rock Mech Rock Eng 14:27–35
Langenbruch C and Shapiro S (2014) Probability of brittle rock failure during hydraulic fracturing of conventional and unconventional reservoirs. In: SEG expanded abstracts, Denver, 2014
Leaney S, Yu X, Chapman C, Bennett L, Maxwell S, Rutledge J, Duhault J (2014) Anisotropic moment tensor inversion and visualization applied to a dual well monitoring survey. CSEG Recorder 39:48–54
Matsunaga I, Kobayashi H, Sasaki S and Ishida T (1993) Studying hydraulic fracturing mechanisms by laboratory experiments with acoustic emission monitoring. Paper presented at the 34th US symposium on rock mechanics, ARMA, Madison, 28–30 June 1993
Mayerhofer M, Lolon E, Warpinski N, Cipolla C, Walser D, Rightmire C (2010) What is stimulated reservoir volume? SPE Prod Oper 25:89–98
Maxwell S, Rutledge J, Jones R, Fehler M (2010) Petroleum reservoir characterization using downhole microseismic monitoring. Geophysics 75:75A129–75A137
Maxwell S, Shemeta J, Campbell E and Quirk D (2008) Microseismic deformation rate monitoring. Paper presented at the SPE annual technical conference and exhibition, Denver, 21–24 Sept 2008
Maxwell S, Urbancic T, Le Calvez J, Tanner K, Grant W (2004) Passive seismic imaging of hydraulic fracture proppant placement. In: SEG Expanded Abstracts, Denver, 2004
McLennan J, Green S, Bai M (2008) Proppant placement during tight gas shale stimulation: literature review and speculation. Paper presented at the 42nd US symposium on rock mechanics, ARMA, San Francisco, 29 June–2 July 2008
Neuhaus C, Ellison M, Telker C, Blair K (2014) Drainage estimation and proppant placement evaluation from microseismic data. Paper presented at the SPE/EAGE European unconventional resources conference and exhibition, Vienna, 25–27 Feb 2014
Roche V, van der Baan M (2015) The role of lithological layering and pore pressure on fluid-induced microseismicity. J Geophys Res 120:923–943
Rutledge J, Phillips W (2003) Hydraulic stimulations of natural fracture as revealed by induced microearthquakes, Carthage cotton valley gas field, east Texas. Geophysics 68:441–452

Rutledge J, Phillips W, Mayerhofer M (2004) Faulting induced by forced fluid injection and fluid flow forced by faulting: an interpretation of hydraulic-fracture microseismicity, Carthage cotton valley gas field, Texas. B Seismol Soc Am 94:1817–1830

Rutledge J, Downie R, Maxwell S, Drew J (2013) Geomechanics of hydraulic fracturing inferred from composite radiation patterns of microseismicity. Paper presented at the SPE annual technical conference and exhibition, New Orleans, 30 Sept–2 October 2013

Rutledge J, Yu X, Leaney S (2015) Microseismic shearing driven by hydraulic-fracture opening: an interpretation of source mechanism trends. Lead Edge 34:926–934

Rutledge J, Weng X, Yu X, Chapman C, Leaney S (2016) Bedding-plane slip as a microseismic source during hydraulic fracturing. In: SEG expanded abstracts, Dallas, 2016

Shapiro S, Audigane P, Royer J (1999) Large-scale in situ permeability tensor of rocks from induced microseismicity. Geophys J Int 137:207–213

Sileny J, Hill D, Eisner L, Cornet F (2009) Non-double-couple mechanisms of microearthquakes induced by hydraulic fracturing. J Geophys Res 114:B08307

Stanchits S, Burghardt J, Surdi A (2015) Hydraulic fracturing of heterogeneous rock monitored by acoustic emission. Rock Mech Rock Eng 48:2513–2527. https://doi.org/10.1007/s00603-015-0848-1

Stanek F, Eisner L (2013) New model explaining inverted source mechanisms of microseismic events induced by hydraulic fracturing. In: SEG expanded abstracts, Houston, 2013

Tan Y, Engelder T (2016) Further testing of the bedding-plane-slip model for hydraulic-fracture opening using moment-tensor inversions. Geophysics 81:KS159–KS168

Urbancic T, Rutledge J (2000) Using microseismicity to map Cotton Valley hydraulic fractures. In: SEG expanded abstracts, Calgary, 2000

Vavryčuk V (2011) Tensile earthquakes: theory, modelling and inversion. J Geophys Res 116:B12320

Vavryčuk V (2015) Moment tensor decompositions revisited. J Seismol 19:231–252

Vera Rodriguez I, Stanchits S, Burghardt J (2017) Data-driven, in-situ, relative sensor calibration based on waveform fitting moment tensor inversion. Rock Mech Rock Eng 50:891–911

Yu X, Rutledge J, Leaney S, Sun J, Pankaj P, Weng X, Onda H, Donovan M, Nielsen J, Duhault J (2015) Integration of microseismic data and an unconventional fracture modeling tool to generate the hydraulically induced fracture network: a case study from the cardium formation. West Central Alberta, Canada. Paper presented at the unconventional resources technology conference (URTeC), San Antonio, 20–22 July 2015

Zhang X, Jeffrey R (2008) Reinitiation or termination of fluid-driven fractures at frictional bedding interfaces. J Geophys Res 113:B08416

Zoback M, Rummel F, Jung R, Raleigh C (1977) Laboratory hydraulic fracturing experiments in intact and pre-fractured rock. Int J Rock Mech Min Sci 14:49–58